Simulations of surface acoustic wave devices built on stratified media using a mixed finite element/boundary integral formulation

S. Ballandras, A. Reinhardt, V. Laude, A. Soufyane, S. Camou, and W. Daniau
LPMO-CNRS, UPR 3203, IMFC, Associé à l'Université de Franche-Comté, 32 Avenue de l'Observatoire, 25044 Besançon Cedex, France

T. Pastureaud, W. Steichen, R. Lardat, M. Solal, and P. Ventura
Temex Microelectronics, 399 route des Crêtes, Boîte Postale 232, 06904 Sophia Antipolis Cedex, France

The demand for high frequency surface acoustic wave devices for modern telecommunication applications imposes the development of devices able to answer the manufacturer requirements. The use of high velocity substrates for which a piezoelectric layer is required to excite and detect surface waves has been widely investigated and requires the implementation of accurate theoretical tools to identify the best combinations of material. The present paper proposes a mixed formulation combining finite element analysis with a boundary integral method to accurately simulate the capability of massive periodic interdigital transducers to excite and detect guided acoustic waves in layered media. The proposed model is exploited for different typical configurations. © *2004 American Institute of Physics.* [DOI: 10.1063/1.1758317]

I. INTRODUCTION

Since the beginning of the 1990s, the growth of the modern telecommunication market and more specially the development of general public cellular phones has generated a high demand in research and development for passive radio-frequency (RF) components such as surface acoustic wave (SAW) filters widely used in these systems. Spectacular advances have been performed concerning the size reduction of the SAW devices for narrow band intermediate frequency filtering (30–300 MHz) as well as wide band RF applications (0.8–2.4 GHz). This was achieved not only because of technology improvements but also because of a very strong effort in the modeling and design of SAW devices, taking properly into account their actual structure to benefit from the optimization of second-order effects (for instance, the shape of the metal strips used in interdigital transducers affects the trapping and diffraction effects of wave propagating under such gratings). Pioneer works were proposed by Blötekjaer, Ingebrigsten, and Skeie[1] for modeling infinite periodic grating capabilities to launch and detect surface waves on any semi-infinite piezoelectric substrate but neglecting the mass loading of the electrodes. Milsom, Reilly, and Redwood[2] then proposed a model of finite length devices composed of any pattern of electrodes (still neglecting the electrode mass loading). Afterwards, the interest in the accurate prediction of the influence of the electrode mass loading has pushed some researchers to develop or to adapt modeling concepts mixing integral formulations based on the knowledge of the Green's function of the substrate (the displacement response of a substrate submitted to a local stress solicitation or vice versa) and numerical computation tools such as finite difference or finite element analyses. Baghai-Wadji *et al.* have proposed in the early 1990s such developments for infinite periodic gratings[3] as well as finite electrode structures.[4] Many improvements have been performed since then, allowing for the

development of versatile and very accurate models as proposed by Ventura, Hode, and Solal,[5] Endoh, Hashimoto, and Yamagushi,[6] or Koskela, Plessky, and Salomaa[7] generally devoted to the theoretical characterization of infinite periodic gratings, providing useful data for design tools based on P-matrix[8] or coupling-of-mode[9] approaches.

At the same time, the need for increasing the frequency operation of such devices has generated studies not only on high velocity surface modes such as leaky SAW on $LiTaO_3$ or $LiNbO_3$ but also on compound substrates, for instance, consisting of a piezoelectric layer (AlN, ZnO, etc.) deposited atop a high acoustic wave velocity material such as diamond-C, silicon carbide, sapphire, silicon, and so on. The multiplication of papers on this topic prevents the citation of all of them but Refs. 10–12 can be considered as representative work in that field. Although models exist for predicting the dispersion behavior of acoustic wave in almost any layered structure,[13,14] very little work was devoted to the theoretical description of excitation and detection of waves on stacked media using massive surface interdigital transducers.

In the present paper, we report on a model based on the theoretical approach proposed by Ventura *et al.* for infinite periodic electrode gratings atop semi-infinite substrates widely described in Refs. 15 and 16 and extended to the simulation of such transducers atop any layered media (assuming flat interfaces between each layer). The electrode contribution is described using a finite element analysis benefiting from all the advances performed in that field.[17] The compound substrate is simulated via its Green's function inserted in the above-mentioned boundary integral method (BIM), here again taking advantage of recent developments devoted to the numerical stabilization of the corresponding calculation.[18] This point is essential when computing the response of a device consisting in piezoelectric, dielectric, or metallic layers[19] with various thicknesses in the range from a
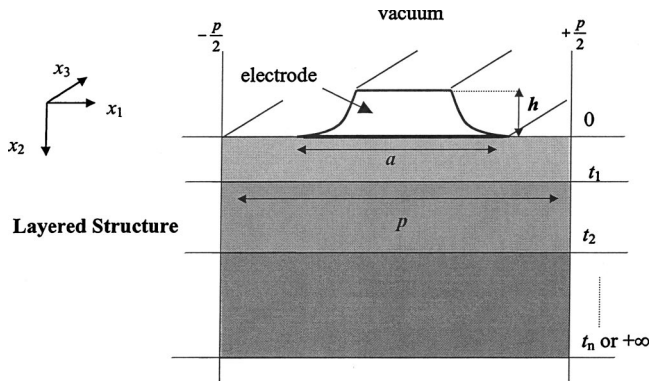
FIG. 1. Scheme of the typical geometry of the addressed problem: an infinite grating of period p along x_1 atop a compound substrate composed of layers stacked along x_2. a/p is the metallization ratio and $h/2p$ the electrode relative height.

few micrometers to a few tenth of nanometers deposited on a semi-infinite or a thick substrate. Both calculations are mixed along the method described in Refs. 15 and 16, allowing for the derivation of the harmonic admittance of the considered structure. One can then extract from this result typical characteristics of the waves that can be excited and detected by the IDTs, such as phase velocity (or slowness), electromechanical coupling, propagation losses, and diffraction of the wave on the electrodes. Although the model can treat intrinsic material losses as imaginary parts of the physical constants, these leakage sources have been neglected in this work. The only leakage phenomena that can occur are then related to wave radiation into the bulk (semi-infinite substrate assumption). In the first section of this paper, we recall the principles of the proposed calculation. Some specific aspects concerning the treatment of the Green's function (and more specifically its asymptotic behavior) are also shown. A second part is devoted to the exploitation of the model for particular layered structures in order to validate our simulation tool and to illustrate its interest for typical layered structures. The propagation modes on typical combinations of layer and substrate are first identified, and a full characterization is provided for optimal working point (frequency-thickness product, ft). Further exploitations and developments of our model are discussed as a conclusion.

II. THEORETICAL APPROACH

A. Harmonic admittance

As mentioned in the Introduction, only the general principles are recalled here since they were already presented in detail in Refs. 15 and 16. We first introduce the basic geometry of the problem, i.e., an infinite periodic grating lying along x_1 deposited atop a compound substrate composed of piezoelectric or metallic layers stacked along x_2 as shown in Fig. 1 (the first layer must be at least dielectric but is generally piezoelectric). Practical interdigital transducers used for the excitation of surface waves generally exhibit apertures large enough to neglect the dependence of the fields along x_3. We assume a spatial harmonic excitation driving the electrode grating, allowing for considering only one period in the formal description of the problem. Using the well established Green's function formalism, the relation between the generalized surface stress $T_{jk} \cdot n_k$ (including the normal electrical displacement as defined in Refs. 15 and 16) and the generalized displacements u_i (including the electrical potential) is given by

$$u_i(x_1) = \int_{-p/2}^{+p/2} G_{ijk}^p(x_1 - x', f) T_{jk}(x') n_k \, dx', \qquad (1)$$

where the periodic Green's function G_{ijk}^p is defined as follows, according to the Floquet theorem combined with the Bloch function:

$$G_{ijk}^p(x_1, f) = \frac{1}{p} \sum_{l=-\infty}^{+\infty} \tilde{G}_{ijk}\left(s_1 = \frac{2\pi}{p}(\gamma + l), f\right)$$
$$\times \exp\left(-j\frac{2\pi}{p}(\gamma + l)x\right) \qquad (2)$$

with f being the frequency, s_1 the slowness along x_1 as defined above, and γ the harmonic excitation parameter.[15,16] The tilde denotes the spectral Green's function and l is the current number of the spatial harmonic of the Bloch-Floquet development. In the following, the normal n_k is considered normal to x_1 without any loss of generality. There is no obvious general analytical solution for Eq. (1). As a consequence, one has to transform the corresponding continuous problem into a discrete form that can be solved using linear algebra techniques. In that matter, we use a Chebyshev development of the generalized displacement and surface stress fields, inserting in the latter the function $1/\sqrt{(1-x^2)}$ accounting for the well-known charge electrode edge effects.[2-7,15,16] This yields the following expressions of T_{2j} and u_i under the electrode:

$$T_{2j}(x_1) = \frac{\sum_{n=-\infty}^{+\infty} \alpha_{jn} C_n(\bar{x}_1)}{\sqrt{1-\bar{x}_1^2}},$$

$$u_i(x_1) = \sum_{n=-\infty}^{+\infty} \beta_{in} C_n(\bar{x}_1),$$

with

$$\bar{x}_1 = \frac{2x_1}{a},$$
$$\qquad (3)$$
$$|x_1| < \frac{a}{2}.$$

In Eq. (3), C_n are the Chebyshev polynomials, and α_{in} and β_{jn} are the development coefficients which become the actual unknowns of the problem. Inserting Eq. (3) into Eq. (1) and then projecting that obtained from over the Chebyshev base provides the relation between the stress and displacement coefficients (α_{in} and β_{jn}) as follows:

$$\beta_{im} = A_{imjn}\alpha_{jn}, \qquad (4)$$

where

J. Appl. Phys., Vol. 96, No. 12, 15 December 2004

Ballandras *et al.*   7733

$$A_{imjn} = \nu_n \frac{\pi^2}{p} j^{m-n} \sum_{l=-\infty}^{+\infty} \tilde{G}_{ij2}(\gamma+l,f)$$

$$\times J_m\left(\frac{\pi a}{p}(\gamma+l)\right) J_n\left(\frac{\pi a}{p}(\gamma+l)\right). \tag{5}$$

In Eq. (5), J_n are the Bessel's functions of nth order and of first kind (also called cylindrical by some authors) and ν_n is a coefficient accounting for the orthogonality properties of the Chebyshev polynomials.[15,16]

Equation (5) then provides $4 \times M$ relations between $8 \times M$ unknowns, requiring then additional equations to solve the problem. They are provided by the boundary conditions imposed at the propagation surface. We consider first the mechanical boundary conditions allowing for the description of massive electrode contribution to the problem. The mechanical stress and displacements are assumed continuous at the electrode/substrate boundary and the normal stresses vanish elsewhere,

$$u_i = L_{ij}(T_{2j}) \quad \text{for } |x_1| < \frac{a}{2},$$

$$\tag{6}$$

$$T_{2j} = 0 \quad \text{for } \frac{a}{2} < |x_1| < \frac{p}{2}.$$

According to Ref. 16, the mechanical behavior of the electrode is simulated using a finite element analysis (FEA) consisting in the calculation of the displacement at the interface electrode/substrate for each term of the Chebyshev development and for each surface stress component. Assuming the restriction of the FEA solution at the above-mentioned interface written as $[K_{ij} - \omega^2 M_{ij}]_\Gamma^{-1}$, one can establish the relation between α_{in} and β_{jn} generated by the electrode as follows:

$$\beta_{im} = D_{imjn}\alpha_{jn} \quad \text{with } i,j = 1,2,3 \tag{7}$$

and

$$D_{imjn} = \left[\int P_m C_q\right][K_{ij} - \omega^2 M_{ij}]_\Gamma^{-1}\left[\int P_n C_k\right], \tag{8}$$

where ω is the angular frequency and the matrix $[\int P_m C_q]$ symbolically holds for the integration of the product of FEA interpolation and Chebyshev polynomials when mixing the FEA and the boundary integral formulation of Eq. (1). Equation (7) then provides $3 \times M$ more equations to the $4 \times M$ ones previously established in Eq. (4). Finally, an electric boundary condition is imposed, considering the flat electrode assumption conformably to Refs. 2–7, 15, and 16. It consists in setting the electrode to a 1 V excitation potential, fixing then the corresponding M Chebyshev development coefficients as follows:

$$\beta_{40} = 1 \quad \text{and} \quad \beta_{4m} = 0 \quad \text{for } m \neq 0. \tag{9}$$

As in Refs. 15 and 16, the linear system constructed with Eqs. (4), (7), and (9) is solved using standard linear algebraic equation tools. One can then have access to the harmonic admittance of the structure by computing the total electrical charge Q_{total} under the electrode, taking advantage of the orthogonal properties of Chebyshev polynomials. The har-

monic admittance is computed considering an acoustic aperture equal to twice the grating's period, in order to normalize the frequency by the above-mentioned period (fp). The harmonic admittance YH is then directly expressed in siemens (S). For a unit potential excitation, it reads

$$YH(\gamma,fp) = 2pY(\gamma,fp)$$

$$= j2p\omega Q_{total}$$

$$= j2\pi fp \frac{\pi a}{2}\alpha_{40}. \tag{10}$$

From this harmonic admittance, one can extract general data about the excitation and guiding of any mode of the structure as performed for single-crystal substrates,[15,16] i.e., the velocity, the electromechanical coupling, the propagation leakage, and the wave diffraction due to massive electrodes. Thanks to the use of FEA, no restriction has to be considered about the electrode shape and height.

B. Green's function for layered substrates

In the calculation presented above, only the spectral Green's function has to be computed to simulate any substrate (semi-infinite or of given thickness) thanks to the infinite periodicity of the problem. This considerably simplifies the calculation process since the Green's function of a given compound substrate can be easily derived only in the spectral domain. Moreover, the dispersion behavior of such a substrate would impose the computation of the spatial Green's function (if required) for each frequency by inverse Fourier transform, which would take too long. However, particular care must be devoted to the way the Green's function is computed to avoid numerical instabilities, particularly for the case of a substrate of finite thickness, for thick layers atop semi-infinite substrates, and for stacked layers exhibiting large thickness variations. In these cases, a so-called diffusion-matrix method was proposed in Ref. 18 enabling stable computation of the Green's function of any substrate. The principle of this method is recalled here.

According to Fahmy-Adler approach,[13,20] we consider a state vector $\mathbf{h} = (u_i, T_{2j})^t$ associating the generalized stress and displacement fields to describe the acoustic behavior of each material of the stack by an eigenvalue problem (the superscript t indicates vector or matrix transposition). The stacked structure conforms to the definition of Fig. 2. For a given couple of slowness (s_1, s_3), the state vector for any material of the layer stack can be expressed as the product of a matrix $\mathbf{F}$ composed of the eight corresponding eigenvectors with a diagonal matrix $\Delta(x_2)$ of rank 8×8 describing the dependence along x_2 via the eigenvalues s_2 (Ref. 18) and a vector $\mathbf{a}$ of the partial mode amplitudes,

$$\mathbf{h}(x_2) = \mathbf{F}\Delta(x_2)\mathbf{a}\exp[2j\pi f(t - s_1 x_1 - s_3 x_3)]. \tag{11}$$

For each layer m, an intermediate variable $\mathbf{g}^{(m)}$ is introduced. This vector of same nature and rank as $\mathbf{a}$ allows for the separation of reflected and incident partial waves at the layer interfaces (see Fig. 3),
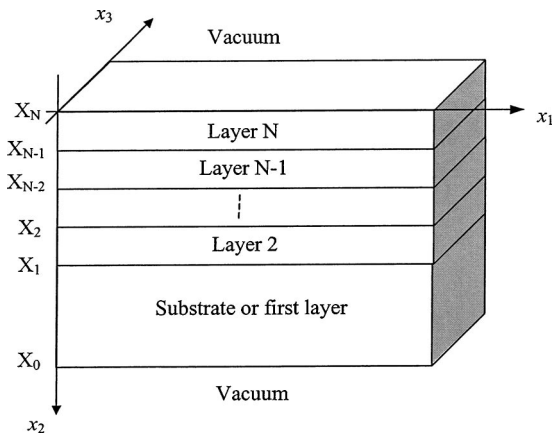
7734   J. Appl. Phys., Vol. 96, No. 12, 15 December 2004

Ballandras *et al.*

FIG. 2. Geometrical definition of a stacked structure for the computation of the corresponding surface Green's function.

$$\mathbf{g}^{(m)}(x_2) = \begin{pmatrix} \mathbf{g}^{(m+)} \\ \mathbf{g}^{(m-)} \end{pmatrix}$$

$$= \mathbf{\Delta}^{(m)}(x_2)\mathbf{a}^{(m)}$$

$$= \begin{pmatrix} \mathbf{\Delta}^{(m+)}(x_2) & 0 \\ 0 & \mathbf{\Delta}^{(m-)}(x_2) \end{pmatrix} \begin{pmatrix} \mathbf{a}^{(m+)} \\ \mathbf{a}^{(m-)} \end{pmatrix}, \qquad (12)$$

where $\mathbf{\Delta}^{(m\pm)}(x_2)$ and $\mathbf{a}^{(m\pm)}$ correspond to the terms of the matrix $\mathbf{\Delta}$ and of the vector $\mathbf{a}$ relative to reflected $(+)$ and incident $(-)$ partial waves. By a matter of fact, one can define a reflection matrix $\mathbf{R}^{(m)}$ of rank 4×4 at the interface between layer $(m-1)$ and layer m linking together incident and reflected partial waves as follows:

$$\mathbf{g}^{(m-)}(X_{m-1}) = \mathbf{R}^{(m)}\mathbf{g}^{(m+)}(X_{m-1}). \qquad (13)$$

In case the first layer is semi-infinite, the reflection matrix $\mathbf{R}^{(1)}$ is null, otherwise the bottom surface is assumed free. In this latter situation, the surface stress and charge density are assumed null (only the generalized surface displacements in vector $\mathbf{h}$ are nonzero), providing the expression of $\mathbf{g}^{(1)}$. Thus, one can compute the reflection matrix $\mathbf{R}^{(1)}$ considering the definition of Eq. (13).[18] Note that the permittivity of the adjacent medium can be taken into account along the process described in Refs. 13, 15, 16, 18, and 19. Once the reflection matrix is known at the first interface, the reflection matrices at the other interfaces of the stack are computed iteratively using a recurrence process. It consists first in linking the interfaces between layers m and $(m+1)$ via the variable $\mathbf{g}$ as follows:

$$\mathbf{g}^{(m)}(X_m) = \mathbf{\Delta}(-t_m)\mathbf{g}^{(m)}(X_{m-1}), \qquad (14)$$

where t_m is the thickness of the layer m conformably to Fig. 2. Using Eq. (13), one can express $\mathbf{g}^{(m)}(X_m)$ only as a function of reflected partial waves, yielding the following expression:

$$\mathbf{g}^{(m)}(X_m) = \begin{pmatrix} I_4 \\ \mathbf{\Delta}^{(m-)}(-t_m)\mathbf{R}^{(m)}\mathbf{\Delta}^{(m+)}(t_m) \end{pmatrix}$$

$$\times \mathbf{\Delta}^{(m+)}(-t_m)\mathbf{g}^{(m+)}(X_{m-1}). \qquad (15)$$

In Eq. (15), I_4 is the identity matrix of rank 4×4. The continuity of the generalized normal stresses and displacements at the interface between layers m and $(m+1)$, i.e., the equality of state vectors $\mathbf{h}^{(m+1)}(X_m)$ and $\mathbf{h}^{(m)}(X_m)$, provides the relation between $\mathbf{g}^{(m+1)}$ and $\mathbf{g}^{(m)}$ which reads

$$\mathbf{g}^{(m+1)}(X_m) = [\mathbf{F}^{m+1}]^{-1}\mathbf{F}^{(m)}\mathbf{g}^{(m)}(X_m). \qquad (16)$$

Equation (15) can be now inserted into Eq. (16), yielding the definition of a matrix of rank 8×4 in which two submatrices $\mathbf{K}$ and $\mathbf{L}$ can be emphasized, relative to reflected and incident partial waves of layer $(m+1)$, respectively,

$$[\mathbf{F}^{m+1}]^{-1}\mathbf{F}^{(m)}\begin{pmatrix} I_4 \\ \mathbf{\Delta}^{(m-)}(-t_m)\mathbf{R}^{(m)}\mathbf{\Delta}^{(m+)}(t_m) \end{pmatrix} = \begin{pmatrix} \mathbf{K} \\ \mathbf{L} \end{pmatrix}. \qquad (17)$$

Conformably to Eq. (13) one can finally deduce the reflection matrix of layer $(m+1)$ as $\mathbf{R}^{(m+1)} = \mathbf{L}\mathbf{K}^{-1}$. This iterative scheme is repeated until the top layer of the stack is reached (i.e., $x_2 = X_N$ as defined in Fig. 2). The state vector $\mathbf{h}$ relative to the top surface then reads

$$\mathbf{h}(X_N) = \mathbf{F}^{(N)}\mathbf{g}^{(N)}(X_N)$$

$$= \mathbf{F}^{(N)}\begin{pmatrix} I_4 \\ \mathbf{\Delta}^{(N-)}(-t_N)\mathbf{R}^{(N)}\mathbf{\Delta}^{(N+)}(t_N) \end{pmatrix}$$

$$\times \mathbf{g}^{(N+)}(X_N)$$

$$= \begin{pmatrix} \mathbf{N} \\ \mathbf{P} \end{pmatrix}\mathbf{g}^{(N+)}(X_N). \qquad (18)$$

Introducing $\mathbf{N}$ and $\mathbf{P}$ as submatrices relative to the generalized surface displacements and stresses, respectively, one can define the spectral Green's function relating u_i to T_{2j} as $\mathbf{G} = \mathbf{N}\mathbf{P}^{-1}$ [where $\mathbf{G}$ is a matrix of rank 4×4 corresponding to the G_{ij2} tensor of Eq. (5)], conformably to the usual process for semi-infinite substrates.[2–7,15,16]
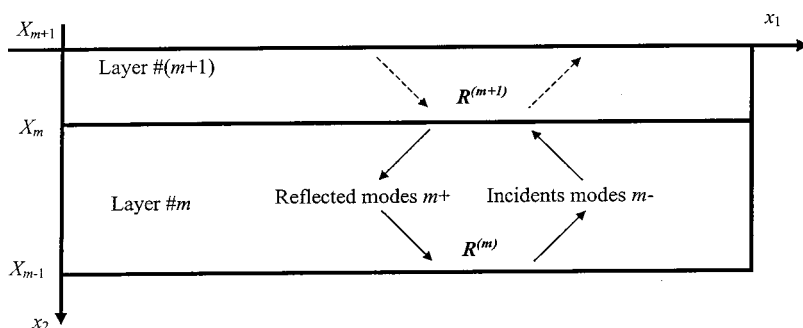

FIG. 3. Recurrence principle—definition of the reflected and incident modes.

C. Numerical aspects

An important point to note concerns the fact that in the above-described recurrence process, all the inverted matrices are nonsingular in the most general case. Particularly, for large values of the frequency-slowness-thickness product ($\omega s_2 t_m$) in matrix Δ, the associated submatrices relative to reflected and incident partial waves tend to zero and do not degrade the algorithm stability. This is obviously a strong advantage of the partial waves' separation.

In Eq. (5), one assumes infinite summation of the spatial harmonics that cannot be practically performed. Consequently, a description of the asymptotic behavior of the Green's function is used conformably to the one proposed by Ventura (see Ref. 15 for a comprehensive description of the calculation). Actually the first layer of the stacked substrate may appear as a semi-infinite material for large enough values of slowness. In that case, one can substitute the corresponding Green's function to the one of the actual compound substrate for the computation of the asymptotic Green's function coefficients. The infinite summation of spatial harmonics can be then truncated to a given value L ($-L-1 < l < L$, for instance, $L=10$ provides accurate and stable results). However, due to the possible large differences between the substrate layers' thickness, one has to implement stable algorithms for accurately computing the Green's function, especially for large values of slowness which exacerbates the above-mentioned differences.[18]

Also the number of terms in the Chebyshev developments has to be set to a given value M. Practically, the restriction of the developments to ten terms consists in a satisfying trade-off between computation duration and accuracy, as in the case of single-crystal semi-infinite substrates.[15,16] A smaller value yields inaccurate results, whereas over-dimensioned value of M (for instance, M greater than 30) generates numerical instabilities.

III. EXPLOITATION OF THE MODEL

Once the model is implemented numerically, one can exploit it to identify optimal working configurations on any compound substrate. To illustrate that procedure, typical combinations of material are considered along the following procedure. We first compute the dispersion curve of the compound considered using the Green's function. This provides the evolution of the mode velocities and coupling coefficients versus the normalized frequency-thickness (ft) product. The coupling coefficient K_s^2 then is given by the ratio $2(V_{free} - V_{met})/V_{free}$ with V_{free} and V_{met} the wave velocity, respectively, assuming a free and a metallized surface. Both values are deduced from the effective permittivity that is inversely proportional to the G_{442} term of the Green's function. We then focus on the most favorable ft working points for computing a full set of relevant excitation and propagation parameters of selected modes, i.e., phase velocity, coupling strength (here defined as the ratio between the amplitude of the pole of the mode and the static capacitance), reflection coefficient on a single strip, and propagation leakage. Concerning the latter parameter, we principally look for nonleaky modes. Consequently, it is generally not plotted
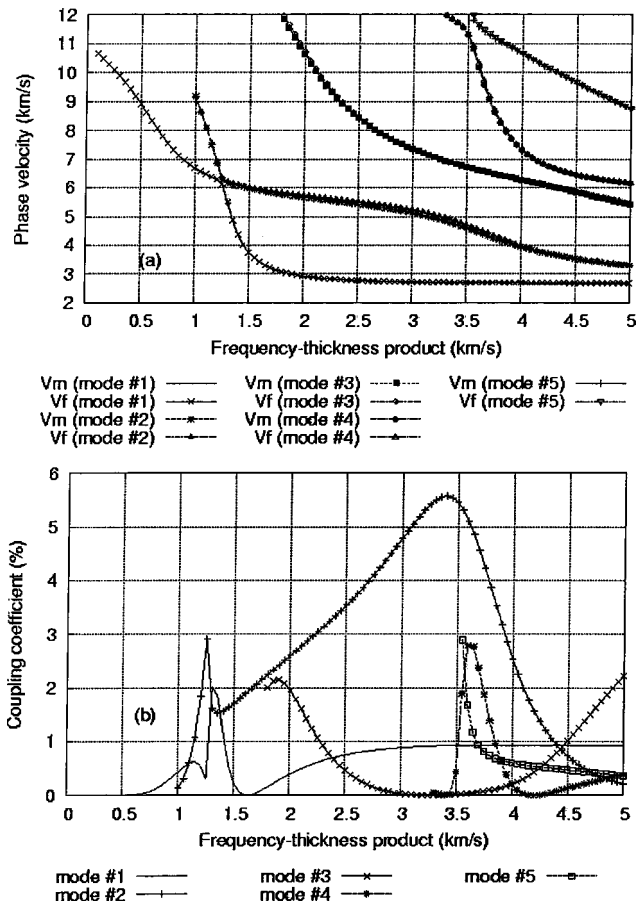

FIG. 4. Dispersion curve for the ZnO/C-diamond configuration for the five first modes. (a) Phase velocities (V_m metallized surface, V_f free surface), (b) electromechanical coupling factors.

and simply indicated when not identically equal to zero. Note that the coupling strength is comparable with the coupling coefficient, but more general since it can apply to the above definition for leaky modes. The coupling strength also accounts for the dynamic capacitance changes whereas the coupling factor K_s^2 is a static parameter.

A. ZnO/C-diamond

Zinc oxide is one of the most often used piezoelectric layers to excite guided waves on nonpiezoelectric substrates.[10,12] It is obtained by reactive RF sputtering of zinc using an oxygen plasma to promote the oxidation phenomenon. To the best of our knowledge, it can be easily deposited on a large number of substrates. ZnO belongs to the 6 mm class of hexagonal materials and grows along its C axis using most of the standard sputtering deposition processes. The use of diamondlike carbon for surface acoustic wave engineering has been imagined as soon as such substrate and thin piezoelectric layers became available. As for ZnO, the diamond layer is assumed C oriented (i.e., the C axis is normal to the surface) and is identified as a $(YXl)/90°$ in the IEEE Std-176 standard (1949). With bulk acoustic wave velocities ranging from 12 000 to 20 000 m s^{-1}, it appears as a very attractive material for RF applications. Figure 4 shows the dispersion curve for the first modes of the waveguide. One can note from this graph that for ft smaller than
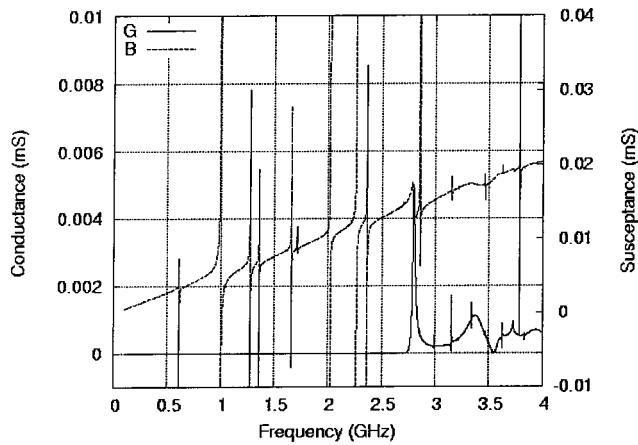
FIG. 5. Harmonic admittance of a 3.4 μm thick ZnO layer atop C-diamond. Grating period 2.35 μm, excitation parameter $\gamma = 0.5$, $h/2p = 1\%$, $a/p = 50\%$.

1 km s^{-1} (or 1 GHz μm), no wave can be efficiently excited. The most interesting working should be found in the range 2.5–3.5 μm because the second mode is then found well coupled (K_s^2 in the range 3%–5%) and the phase velocity appears almost stable with ft variations. The main drawback of such a configuration is the occurrence of a non-negligible contribution of the first mode, the third one almost vanishing (K_s^2 smaller than 0.1%) at $ft = 3.3$ km s^{-1}. Note that the fifth mode can reach an electromechanical coupling larger than 4% at $ft = 3.5$ km s^{-1} (phase velocity equals 12 300 m s^{-1}), but the dependence of the velocity versus ft was judged too large for any actual implementation as well as the spectral distribution density. One can actually note that the fourth and fifth modes behave similarly to the first and second ones when their velocities become very close. All the regarded modes are free of any propagation leakage.

The analysis of an infinite periodic aluminum grating's acoustic-electric properties is then performed for $ft = 3.4$ km s^{-1} for which the coupling of the second mode reaches 5.5% and the mode separation sufficient to enable efficient computations.[16] Also it may be acceptable to deposit, for instance, a 2 μm thick ZnO layer for devices operating at 1.6–1.8 GHz. Above that value of ft, the coupling of the second mode dramatically drops and the two first modes tend to mix together. In our calculations, we have fixed the thickness of the ZnO layer to 3.4 μm, yielding a grating's period of 2.35 μm corresponding to an expected wave velocity close to 4700 m s^{-1} (working frequency in the vicinity of 1 GHz). The aluminum is assumed isotropic and the shape of the electrode is assumed rectangular. Its relative height $h/2p$ and metallization ratio a/p are varied in the respective ranges 1%–5% and 30%–80%. Figure 5 shows an example of the harmonic admittance computed for $\gamma = 0.5$ (alternated $+V/-V$ excitation figure), $h/2p$ and a/p being, respectively, fixed to 1% and 50%. Among the tremendous number of guided modes (indicated by the poles of the harmonic susceptance, i.e., the sharp variations of the curve versus frequency), a major contribution is actually found at 1 GHz and also less coupled contributions of other modes as previously predicted. This figure also confirms the absence
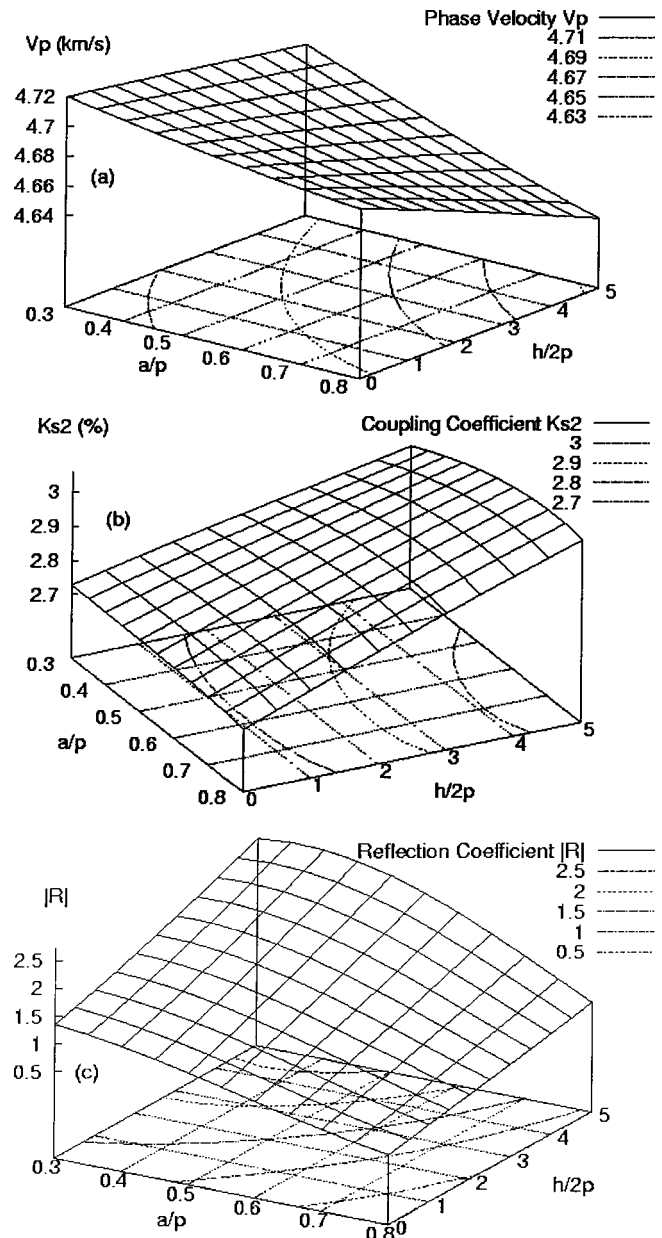

FIG. 6. Characterization of the second mode of the ZnO/C-diamond compound vs electrode shape (relative height $h/2p$ and metallization ratio a/p). ZnO thickness 3.4 μm, grating period 2.35 μm. (a) Phase velocity, (b) electromechanical coupling strength, (c) magnitude of the reflection coefficient on one aluminum strip.

of leaky propagation (harmonic conductance G is negligible) until the velocity threshold of bulk radiation in C-oriented diamond (i.e., 12 807 m s^{-1}).

The wave velocity as well as the coupling strength and the reflection coefficient on one aluminum strip are then extracted according to Ref. 15, and the results are reported in Figs. 6(a)–6(c). As in the case of single-crystal substrates, the wave velocity is strongly affected by the mass loading effect and then exhibits a quadratic decrease along $h/2p$ and a/p. However, one can note that surprisingly the coupling strength never reaches the value of 5% found using K_s^2 derived from the effective permittivity and remains smaller than 3%, even if no mass loading is considered. This phenomenon does not occur for the first mode (coupling strength
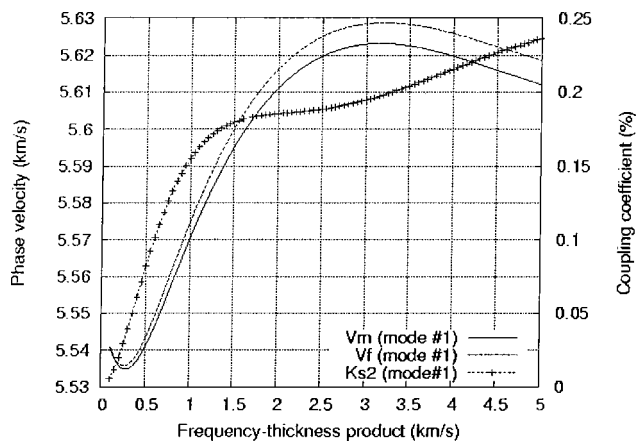
FIG. 7. Dispersion curve of the first mode for the AlN/sapphire configuration (phase velocities and electromechanical coupling factor).

found close to 0.93% when computed using the harmonic admittance) and may be explained by a distortion of the mode shape due to the actual charge distribution over the electrode. On the other hand, one can expect a larger coupling coefficient when increasing the electrode thickness at the price of a dramatic reduction of the phase velocity (which is already comparable to the phase velocity on LiNbO$_3$ (YXl)/64° in that configuration). Nevertheless, one can note that the propagation leakages are homogeneously equal to zero for all the considered electrode shapes. Another interesting aspect of this configuration is that the maximum of the reflection coefficient magnitude $|R|$ is found for small

metallization ratio, contrary to the case for most of the single-crystal substrates.[5,15,16,21] Such a feature is very important for the fabrication of actual devices and cannot be accessed without an advanced simulation tool as the one described and used here. Finally, the directivity factor remains always smaller than 0.1°, indicating that the resonance always occurs at the beginning of the frequency stop band (no resonance arises at its end).

B. AlN/Sapphire

The analysis of the effective permittivity enables one to extract the propagation parameters of two coupled modes, but only one is free of propagation leakages (the second one exhibits losses up to 1 dB/λ which is not compatible with practical surface wave device implementation). This is mainly due to the fact that waves propagate in the AlN layer with a phase velocity generally larger than the cutoff velocity corresponding to bulk wave radiation in sapphire. The dispersion of this mode is reported in Fig. 7. We then only focus on the first mode for which a zero dependence of the phase velocity versus the ft product can be found in the range 3–3.5 km s^{-1}. The FEA/BIM computation is then performed for $ft = 3.25$ km s^{-1} and the grating's period was fixed to 2.8 μm in order to operate close to 1 GHz.

Figures 8(a)–8(d) show the evolution of the phase velocity, the coupling strength, and the reflection coefficient on one aluminum strip. In that case, the coupling strength is in good agreement with the coupling factor obtained from the Green's function, but one can see that it dramatically reduces
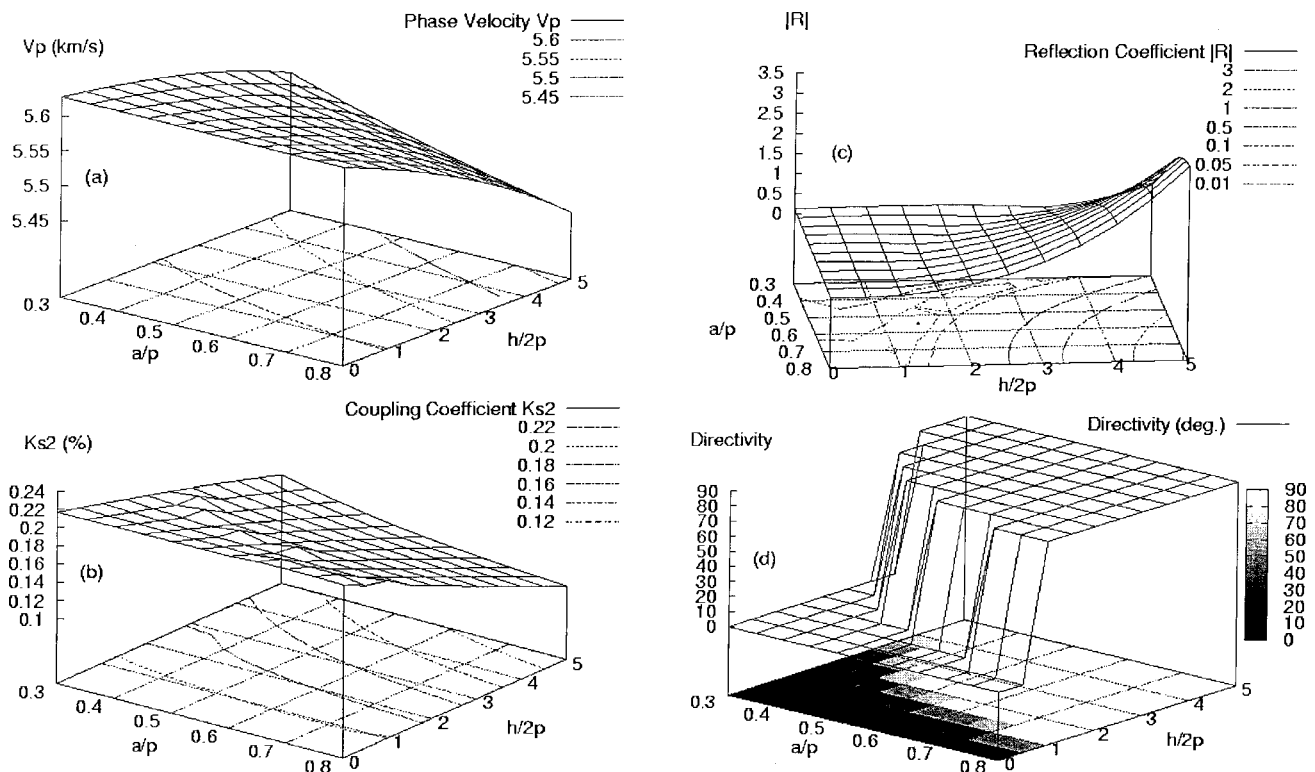

FIG. 8. Characterization of the first mode of the AlN/sapphire compound vs electrode shape (relative height $h/2p$ and metallization ratio a/p). AlN thickness 3.25 μm, grating period 2.8 μm. (a) Phase velocity, (b) electromechanical coupling strength, (c) magnitude of the reflection coefficient on one aluminum strip, (d) directivity.

with the mass loading. Another interesting point concerns the reflection coefficient that changes its sign when the electrode reaches a given shape (a/p times $h/2p$). Under that threshold, the resonance occurs at the beginning of the frequency stop band and at the end above it. This is characterized by the change in the directivity (the capability of the transducer to generate more electroacoustic energy on one side than the other; see, for instance, Refs. 15 and 21 for a comprehensive definition of the phenomenon) which abruptly varies from 0° to 90°. A similar phenomenon was already pointed out for the Rayleigh wave on $(YXl)/128°$ lithium niobate.[21] Note that large reflection coefficients are obtained above $h/2p = 3\%$ to the price of a severe reduction in the electromechanical coupling. Finally, a stability point of the reflection coefficient (corresponding amplitude from 0.1 to 0.13) is observed for small a/p and $h/2p$. Such a configuration is attractive only for delay lines which requires almost no reflection by the grating. One can then take advantage of the weak reflection and operate using standard finger width ($\lambda/4$) instead of split fingers hardly achievable at high frequencies. Whatever, this solution suffers from a lack of coupling for filter application but may be attractive when using heavy metallization for resonators. The problem here is the linear thermal dependence of the frequency which weaken the solution compared to quartz for instance.

C. LiNbO$_3$/(100) Silicon

In this case, the lithium niobate layer is assumed to be deposited using sputtering techniques, yielding a C-oriented film. This corresponds to a $(YXl)/90°$ cut conformably to the IEEE standard Std-176. Only the propagation along the X axis is considered for the sake of conciseness. The silicon corresponds to a (YX) cut. The propagation parameters of the fourth first modes are extracted from the effective permittivity as previously and reported in Fig. 9. Propagation loss is always smaller than 10^{-4} dB/λ. The second mode is particularly interesting, exhibiting an electromechanical coupling above 6% at $ft = 1.3$ km s^{-1}. This is the working point for which the FEA/BIM analysis is performed as for the previous cases. Note that the coupling of the third mode tends to increase with increasing ft values when this mode comes near the second one. However, possible mixing of modes and also the large values of ft prevent the practical use of such a mode.

The FEA-BIM calculation results are reported in Figs. 10(a)–10(c). Note that in this case, the coupling strength extracted from the harmonic admittance is also in good agreement with the electromechanical coupling coefficient computed using the effective permittivity (in the vicinity of 6%). This coefficient increases along the electrode height and slightly higher values of coupling strength should be reached for larger mass loading. The metallization ratio a/p corresponding to a maximum coupling factor is small for thin metal thickness and moves to larger values for large electrode height (0.75 at $h/2p = 5\%$). A similar evolution is observed for the reflection coefficient $|R|$, but the optimum value is rather found at $a/p = 0.5$ for $h/2p = 5\%$. Since the variation of the coupling strength versus a/p is weak for
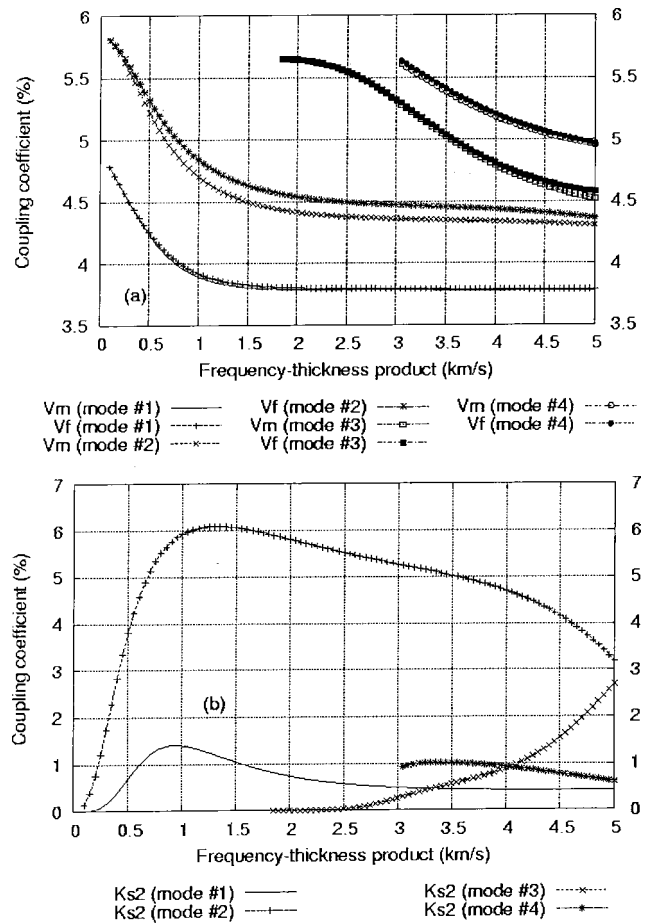

FIG. 9. Dispersion curve for the LiNbO$_3$/(100) silicon configuration for the five first modes. (a) Phase velocities (V_m metallized surface, V_f free surface), (b) electromechanical coupling factors.

such an electrode height, it sounds better to optimize $|R|$ and to take advantage of the inversion point of its dependence versus the metallization ratio. As for ZnO/diamond (Sec. III A), there is no directivity effects, and the resonance always arises at the beginning of the frequency stop band.

D. LiNbO$_3$/C-diamond/(100) Silicon

Finally a more complicated case is addressed to fully illustrate the capability of the proposed model. It consists in a thin LiNbO$_3$ film deposited atop a thick diamondlike carbon layer above a semi-infinite (100) silicon substrate. This combination of material has been already tested and provides an attractive solution for very high frequency large band filtering applications.[22] Here, the carbon layer thickness was arbitrarily fixed to 20 μm but of course a comprehensive optimization of this configuration would require to vary this parameter too. For the present illustration, the ft product only holds for the LiNbO$_3$ layer. As in the case of ZnO/C-diamond (Sec. III A), many modes are found close to each other (see Fig. 11), but the third one exhibits particularly attractive properties, with a large coupling coefficient (up to 18%) and a high phase velocity (about 10^4 m s^{-1}) for an ft product close to 1.3 km s^{-1}. This point has been then selected for the FEA-BIM characterization, even if the phase velocity is found highly dependent on the layer's thickness.
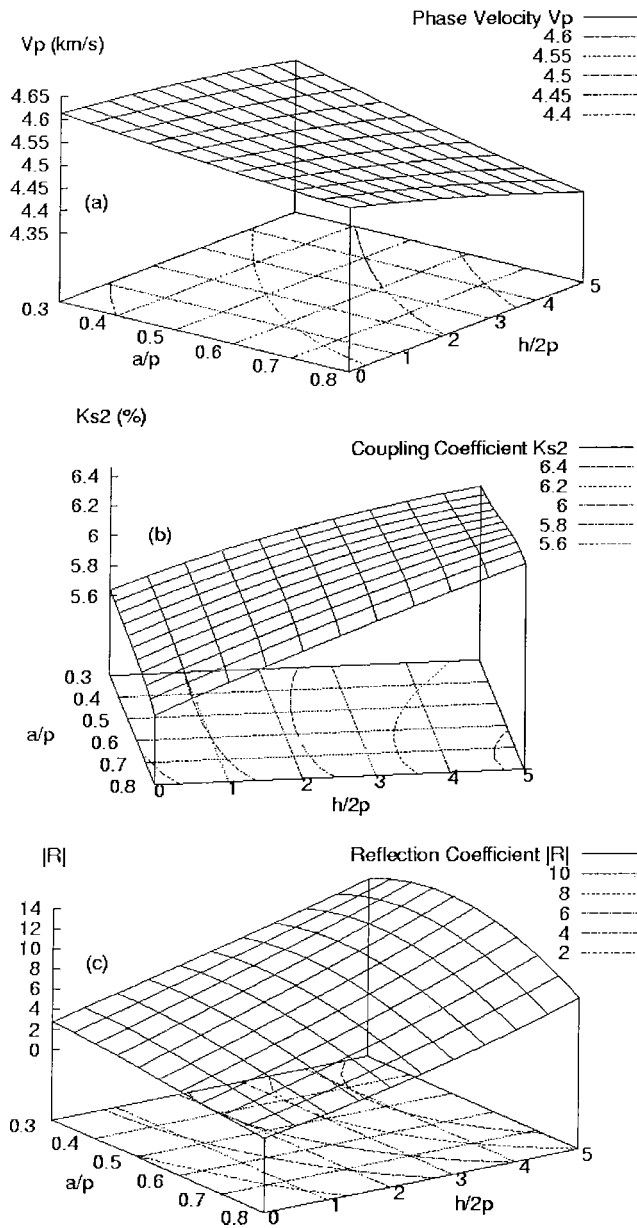
FIG. 10. Characterization of the second mode of the LiNbO₃/(100) silicon compound vs electrode shape (relative height $h/2p$ and metallization ratio a/p). LiNbO₃ thickness 1.3 μm, grating period 2.3 μm. (a) Phase velocity, (b) electromechanical coupling strength, (c) Magnitude of the reflection coefficient on one aluminum strip.

FIG. 11. Dispersion curve for the LiNbO₃/C-diamond/(100) silicon configuration for the four first four modes. (a) Phase velocities (V_m metallized surface, V_f free surface), (b) electromechanical coupling factors.

Actually, considering technology limits, the use of such compound substrate allows for the fabrication of 5 GHz devices with a grating period of 1 μm, which is out of reach for any single piezoelectric crystal. In the following calculations, the period was fixed to 5 μm for the sake of comparison with the other treated cases.

As in the previous cases, the phase velocity, coupling strength, and reflection coefficient (as well as the directivity) have been computed for $0.3 < a/p < 0.8$ and $h/2p$ varying from 0% to 5%. Figures 12(a)–(c) present the mapping of these characteristics along these parameters. The propagation leakages are homogeneously equal to zero for all the considered couples ($h/2p,a/p$). As in the case of ZnO/diamond (Sec. III A), the coupling strength is found to be about twice
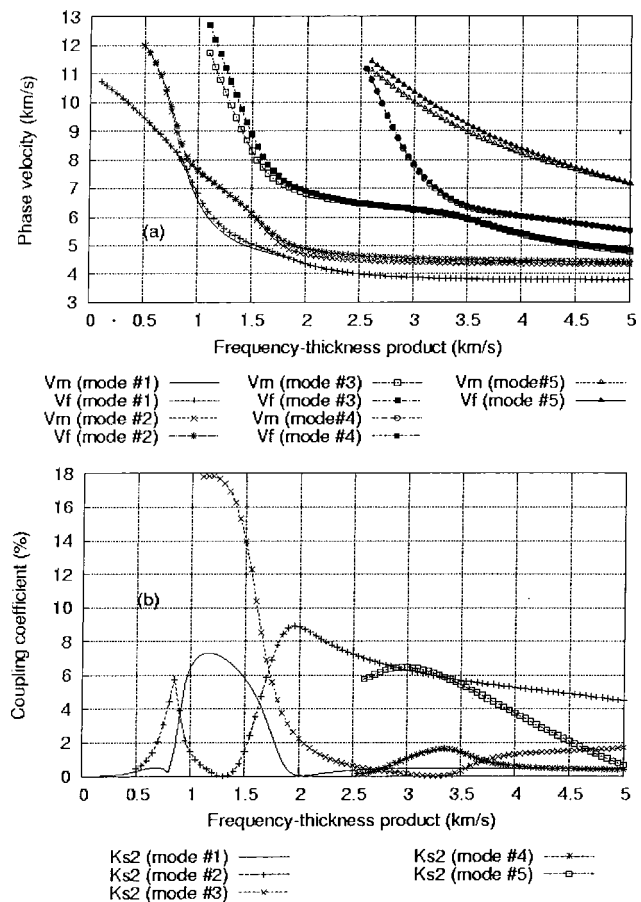
as small as expected considering results extracted from the effective permittivity. The metallization ratio $a/p = 0.5$ which is the most commonly used when developing prototype SAW in a blind approach is found the less favorable case in terms of coupling strength (this of course is not an intuitive result). When also regarding the reflection coefficient $|R|$, one can easily deduce that the preferred configuration on such compound corresponds to small values of a/p (typically 0.3–0.35). A coupling strength of 8.7% can be reached for $a/p = 0.3$ and $h/2p = 5\%$ with a velocity close to 9500 m s⁻¹. These figures are particularly well suited for present and future RF wide band filtering applications. For those who have access to diamond and LiNbO₃ layer technologies,[22] it is a possible alternative to the development of bulk acoustic wave (BAW) AlN-based thin film resonators,[23] which exhibit comparable features considering the phase velocity and coupling factor.

E. Discussion

As we tried to show along with the presented illustrations, the evolution of wave characteristics under periodic gratings may significantly differ from the data extracted from the effective permittivity or any equivalent approach. In such models, severe assumptions concerning the propagation conditions of the wave may generate considerable missestimat-
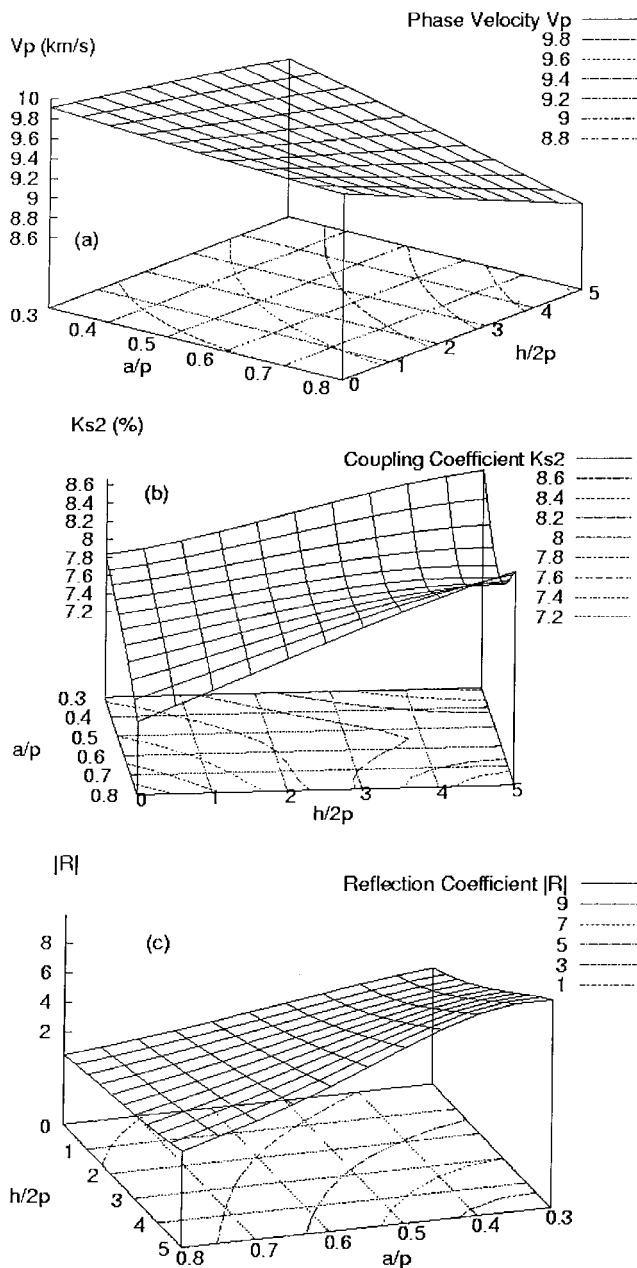
FIG. 12. Characterization of the third mode of the LiNbO$_3$/C-diamond/(100) silicon compound vs electrode shape (relative height $h/2p$ and metallization ratio a/p). LiNbO$_3$ thickness 1.35 μm, C-diamond thickness 20 μm, grating period 5 μm. (a) Phase velocity, (b) electromechanical coupling strength, (c) magnitude of reflection coefficient on one aluminum strip.

ing of the wave characteristics as shown for the electromechanical coupling and also for the impact of the electrode shape on the reflection coefficient. Note that, in any case, the coupling strength is also affected by the width and height of the strip. The observed dramatic fall off of the electromechanical coupling only happens for the diamond based substrate (see Secs. III A and III D). We are not able to propose any clear explanation of that phenomenon yet. The observation of the mechanical displacement and electrical potential distribution in the compound wave guide (including the electrodes) may provide more information about it and should be performed in future developments. The analysis of the mode

distribution computed using the Green's function approach does not reveal any particular difference between the treated waveguides and the polarization of the wave is either elliptic (Sec. III A) or mainly transverse (Sec. III D). Whatever the origin of the phenomenon, the presented examples show that for such complicated associations of material, one cannot avoid an accurate and realistic analysis of the waveguide properties to optimize any SAW device built on those compound substrates.

IV. CONCLUSION

A model combining periodic FEA and a boundary integral method has been developed and implemented to address the problem of elastic waveguides based on interdigital transducers deposited atop layered substrates. In the proposed model, the number of layers and their geometrical characteristics are not restricted because of the effort developed to ensure the stability of the Green's function computations required to describe the acoustic behavior of the compound substrate. The only restriction concerns the interfaces between the layers which have to be flat by construction of the model. Many features of the proposed theoretical approach were not developed here avoiding a too long description, but one can note that a finite thickness substrate can be considered and also one can force the electrical potential at the above-mentioned interface, for instance. It has been demonstrated throughout the paper that the optimization of an acoustic waveguide on compound substrates is not intuitive and strongly depends on material combinations. In that matter, one cannot save the development of such accurate models. It has been demonstrated these passed years that it is a key point in SAW industry. It is also necessary to point out that accurate predictions of SAW characteristics can be achieved only if reliable material coefficients are available. As these coefficients can change considering the bulk and the thin layer configurations, the proposed model also can be used to update material constants taking into account the actual structure of the regarded device (particularly the contribution of the electrodes on the wave signatures). Future developments are expected to provide predictions on temperature stability of acoustic wave devices built on stratified media.

[1] K. Blötekjaer, K. A. Ingebrigsten, and H. Skeie, IEEE Trans. Electron Devices **ED-20**, 1133 (1973).
[2] R. Milsom, N. H. C. Reilly, and M. Redwood, IEEE Trans. Sonics Ultrason. **SU-24**, 147 (1977).
[3] H. Reichinger and A. R. Baghai-Wadji, Proc.-IEEE Ultrason. Symp. **1992**, 7.
[4] H. P. Zideck, A. R. Baghaï-Wadji, and O. Manner, Proc.-IEEE Ultrason. Symp. **1993**, 149.
[5] P. Ventura, J. M. Hode, and M. Solal, Proc.-IEEE Ultrason. Symp. **1995**, 263.
[6] G. Endoh, K. Hashimoto, and M. Yamagushi, Jpn. J. Appl. Phys. **34**, 2638 (1995).
[7] J. Koskela, V. P. Plessky, and M. M. Salomaa, IEEE Trans. Ultrason. Ferroelectr. Freq. Control **45**, 439 (1998).
[8] G. Tobolka, IEEE Trans. Sonics Ultrason. **SU-26**, 6 (1979).
[9] P. V. Wright, Proc.-IEEE Ultrason. Symp. **1989**, 141.
[10] D. L. Dreifus, R. J. Higgins, R. B. Henard, R. Almar, and L. P. Solie, Proc.-IEEE Ultrason. Symp. **1997**, 191.
[11] F. S. Hickernell, Int. J. High Speed Electron. Syst. **10**, 603 (2000).

J. Appl. Phys., Vol. 96, No. 12, 15 December 2004

Ballandras *et al.* 7741

[12] H. Nakahata, A. Hachigo, K. Itakura, S. Fujii, and S. Shikata, Proc. IEEE International Frequency Control Symp. **2000**, 315.

[13] E. L. Adler, IEEE Trans. Ultrason. Ferroelectr. Freq. Control **37**, 485 (1990).

[14] P. M. Smith, IEEE Trans. Ultrason. Ferroelectr. Freq. Control **48**, 171 (2001).

[15] P. Ventura, J. M. Hodé, J. Desbois, and M. Solal, IEEE Trans. Ultrason. Ferroelectr. Freq. Control **48**, 1259 (2001).

[16] Y. Fusero, S. Ballandras, J. Desbois, J. M. Hodé, and P. Ventura, IEEE Trans. Ultrason. Ferroelectr. Freq. Control **49**, 805 (2002).

[17] V. Laude, A. Reinhardt, M. Wilm, A. Khelif, and S. Ballandras, IEEE Trans. Ultrason. Ferroelectr. Freq. Control (to be published).

[18] Th. Pastureaud, V. Laude, and S. Ballandras, Appl. Phys. Lett. **80**, 2544 (2002).

[19] A. Reinhardt, Th. Pastureaud, S. Ballandras, and V. Laude, J. Appl. Phys. **94**, 6923 (2003).

[20] A. H. Fahmy and E. Adler, Appl. Phys. Lett. **22**, 495 (1973).

[21] P. Ventura and J. M. Hodé, Proc.-IEEE Ultrason. Symp. **1997**, 139.

[22] E. Dogeche, V. Saudane, X. Lansiaux, D. Rémiens, and T. Gryba, Appl. Phys. Lett. **81**, 1329 (2002).

[23] K. M. Lakin, Proc.-IEEE Ultrason. Symp. **1999**, 895.